Influence of the energy density on the Young modulus and fatigue strength of Inconel 718 produced by L-PBF

Michele Abruzzo[1,a] *, Giuseppe Macoretta[1,b] , Luca Romoli[1,c] and Gino Dini[1,d]

[1]Università di Pisa, Dipartimento di ingegneria Civile e Industriale, Largo Lucio Lazzarino 1, Pisa, PI, Italy, 56122

[a]michele.abruzzo@phd.unipi.it, [b]giuseppe.macoretta@unipi.it, [c]luca.romoli@unipi.it, [d]gino.dini@unipi.it

Abstract. The present work analyses the influence of the energy density on the Young modulus and the fatigue strength of specimens obtained by Laser-Powder Bed Fusion (L-PBF) in Inconel 718. The specimen production and the process parameters taken as variables are described. The bulk and surface properties of the material are studied through static mechanical tests, surface roughness measurements, and fatigue tests. In addition, an approach based on ping tests and laser interferometry is proposed as a more efficient way to calculate the Young modulus of the specimens. The proposed method does not require any preparation of the specimens and allows for a quick and accurate evaluation of the material's Young modulus. The results obtained highlight the influence of the process parameters on the Young modulus and the fatigue strength, suggesting a different usage of the material based on the productivity parameters adopted.

Introduction

Laser-Powder Bed Fusion (L-PBF) is a widely used additive manufacturing technique that allows the production of high-precision and complex three-dimensional objects. The applications of L-PBF are vast, ranging from aerospace to biomedical and automotive industries. However, the mechanical properties of the produced components are highly dependent on the process parameters used. Studies have shown that the process parameters significantly affect the mechanical properties of the produced components [1-7]. For instance, high laser power and low scanning speed result in the formation of larger grains, which increase the ductility and toughness of the material. On the contrary, higher scanning speeds and lower powder bed temperature result in the formation of smaller grains, leading to higher mechanical strength.

In this context, the present work investigates the effects of the energy density on the mechanical properties of Inconel 718. The feasible region of the process, which describes the occurrence of the principal defects characterizing the L-PBF technology (namely lack of fusion and meltpool instability [8, 9]), was defined based on the analytical model proposed by Moda [10]. Several mechanical tests were used to study the Young modulus and High Cycle Fatigue (HCF) behavior of the material. In addition, the influence of the process parameters combination on the surface roughness of the flat specimens was investigated and discussed. Compared to similar studies and standard measurement methods, the study proposes the ping test as an effective and efficient test to quantify the effects of the energy density on the Young modulus of the material, providing a deeper insight into the correlation between the mechanical properties studied and the process parameters adopted. Under the hypothesis that the bulk and surface properties of the material depend on different combinations of physical phenomena involved in the technological process, the aim of the study is to quantify the influence of the process parameters on the mechanical properties of the material, identifying the combinations required for obtaining the desired features.

Specimen production

The specimens were produced using a Renishaw RenAM 500S Flex SLM machine. The machine can deliver a maximum laser beam power equal to 500 W, and several laser beam modulation parameters can be adopted. The material used was a standard Inconel 718 powder, compliant with the ASTM F3055 standard. The powder features a Particle Size Distribution (PSD) ranging from 13 μm to 53 μm (D10 ÷ D90).

All the specimens were printed within a unique batch using a vertical building direction. The hatching region was realized using a stripe scanning strategy and a layer rotation of 67°, while the outer region was realized by employing a standard contour scanning path. The built plate was pre-heated at 170°C to minimize the residual stresses, and the process chamber was filled with argon. The oxygen concentration obtained was lower than 7 ppmw, guaranteeing the absence of oxidation phenomena.

Three different geometries of the specimens were used to realize the mechanical tests. In particular, the round specimens employed for the tensile tests were designed in accordance with the ASTM E8-16 standard, with a gauge diameter of 6 mm. The round specimens used for the High Cycle Fatigue (HCF) tests were designed according to the ASTM E466 standard. Finally, flat specimens with rectangular section (8x3x80 mm) were used for the ping tests to simplify the printing process, reduce the powder consumption, and simplify the test execution.

Process parameters selection.

The process parameters used for the specimen production were obtained by exploiting an extension of the Rosenthal solution [12] for modeling the thermal field produced by the L-PBF process [10]. The present formulation has been successfully validated by Macoretta et al. [11], who demonstrated that process parameters belonging to the so defined L-PBF feasible region produce a material presenting a material density greater than 99.5% in the worst case.

Taking advantage of the mathematical model adopted, the feasible region of the L-PBF process parameters (i.e., the parameters combination leading to a full dense material) can be defined as a function of two dimensionless parameters, namely the normalized speed V^* and the normalized power P^* defined in [10]. In particular, the L-PBF feasible region for the Inconel 718 alloy is reported in Fig. 1. The lower bound of the feasible region is given by the Lack of Fusion (LoF) curve, while the upper bound is given by the keyhole region (extrapolated from literature data). The dashed lines represent meltpools having the same aspect ratio (Iso-Ar).
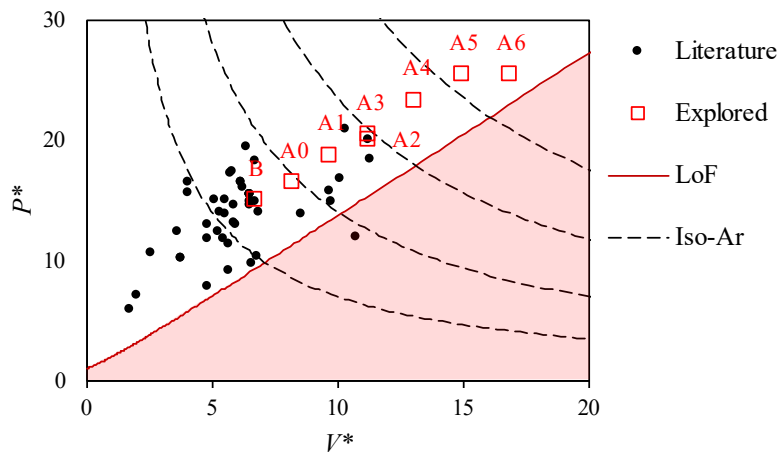

Figure 1: L-PBF process feasible region (white hatched region). Literature data and A_2, A_3, A_5 are obtained from [10] and [11], respectively.

For each parameter combination inside the feasible region, the productivity of the L-PBF process can be calculated as the nominal melted volume per unit of time, neglecting the fixed dwell time

due to the recoater motion. Moreover, the process build rate B_r can be defined as $B_r = t \cdot h \cdot v$ [11], in which t is the layer thickness, h the hatch distance, and v the laser scan speed.

The productivity parameters adopted can also be condensed into an additional parameter and represented using the energy density $E_d = \frac{P}{t \cdot h \cdot v}$, which is defined as the ratio between the laser power P and the nominal melted volume per unit of time.

The final process parameters adopted for the specimen production were obtained starting from the baseline values suggested by Renishaw and already investigated in other studies [13, 14] (hereafter defined as baseline) and moving along a straight line having a similar margin with respect to the lack of fusion region, maintaining a constant layer thickness (hereafter defined as A_i). A total of 8 different configurations were considered (Table 1), with the only exceptions in the proposed logic given by the A_3 and the A_6 process parameters, which were obtained with a higher hatch distance and increasing the scan speed at the maximum deliverable power, respectively. Parameters A_2, A_3, and A_5 are the same adopted in [11]. It is interesting to notice that the process productivity can reach a 150% increase compared to the baseline case.

Table 1. L-PBF process parameters, and process build rate.

	P [W]	v [m/s]	h [μm]	t [μm]	E_d [J/mm³]	B_r [mm³/s]
Baseline	280	0.90	90	60	57.6	4.9
A_0	310	1.10	90	60	51.9	5.9
A_1	350	1.30	90	60	49.9	7.0
A_2	375	1.50	90	60	46.3	7.8
A_3	460	1.50	135	60	45.4	10.1
A_4	435	1.75	90	60	46.0	9.5
A_5	475	2.00	90	60	44.0	10.8
A_6	475	2.25	90	60	39.1	12.2

Surface roughness measurements

The surface roughness of each specimen was measured by a profilometer (Jenoptic Waveline W812R) using a stylus having a tip radius of 2 μm. The measurements were carried out on the top side of the flat specimens (neglecting the effect of the section shape interpolation on surface roughness) at five different positions along their length considering a total measuring window of 15 mm. According to ISO standard 4288:1988, the primary profile obtained was filtered using a Gaussian filter with a cut-off wavelength of 2.5 mm. After filtering, the measured profiles were compared using the arithmetical mean deviation of the profile heights Ra, the mean roughness depth Rz, the skewness Rsk, and the kurtosis Rku, which are reported in Table 2.

As expected, the baseline parameters correspond to the lower value of surface roughness obtainable. On the contrary, increasing the productivity of the SLM process leads to a noticeable increase in surface roughness. Considering the values reported in Table 2, Ra and Rz reach a maximum value for the A_4 process parameters and then undergo a further reduction (plausibly due to the high laser power and scan speed). The skewness is almost null for all the considered specimens, indicating an almost perfectly symmetric distribution of the measured roughness profiles. Depending on the measuring window considered, a higher skewness value (about 1) can be obtained for $E_d = 57.6$ J/mm³ (baseline) and is manifested by a few high-intensity peaks, which are possibly due to residual powder inclusions. The same conclusions can be drawn from the kurtosis analysis of the measured profiles. As the productivity of the process increases, the profile shape shifts from leptokurtic ($R_{ku} > 3$) to mesokurtic ($R_{ku} \approx 3$), indicating that, even if the overall surface roughness is increased, peaks and valleys are evenly distributed.

Table 2. *Surface roughness parameters, mean value and associated standard deviation.*

	Baseline	A_0	A_1	A_2	A_3	A_4	A_5	A_6
Ra [µm]	7.2 ± 0.8	10.3 ± 1.4	11.4 ± 0.9	14.1 ± 1.1	16.2 ± 1.2	17.0 ± 1.3	13.3 ± 0.9	12.8 ± 1.8
Rz [µm]	50.9 ± 2.8	71.2 ± 4.3	71.7 ± 7.3	84.1 ± 7.6	91.6 ± 3.2	98.6 ± 8.5	92.1 ± 10.1	80.2 ± 12.0
Rsk [-]	0.41 ± 0.36	0.21 ± 0.03	0.03 ± 0.05	0.31 ± 0.15	0.23 ± 0.15	0.30 ± 0.10	0.25 ± 0.08	0.39 ± 0.13
Rku [-]	3.56 ± 0.71	3.27 ± 0.39	2.75 ± 0.18	2.88 ± 0.29	2.67 ± 0.21	2.72 ± 0.17	3.08 ± 0.40	3.04 ± 0.21

Mechanical tests

A series of mechanical tests were used to characterize the mechanical properties of the specimens obtained by L-PBF. In particular, the Young modulus of the material E obtained with several process parameters was measured using tensile and ping tests, using the energy density E_d as the main process parameter for the results comparison. The fatigue strength was calculated through a series of High Cycle Fatigue (HCF) tests.

The results of the tensile and HCF tests refer to [11]. Compared to the aforementioned study, the proposed work proposes a new method for identifying the Young modulus, featuring higher accuracy and sensitivity. Furthermore, four additional process parameter combinations are considered, and the relationship between all the mechanical properties of the printed material is investigated, highlighting the coherence of the results obtained.

Tensile tests.

Tensile tests were performed in displacement control on an MTS servo-hydraulic machine (load capacity of 50 kN) at room temperature. At least 3 specimens were tested for each combination of the technological parameters considered. The deformation of the specimens was measured using an extensometer featuring a gauge length of 10 mm (MTS 634.21-F25). In the tensile tests, the Young modulus of the material was calculated as the angular coefficient of the line tangent to the elastic region of the stress-strain curve (up to a maximum stress value of 1/5 of the yield strength).

Ping tests.

The ping test consists in the application of an impulsive excitation to the specimen through an impact tool and in the measurement of the subsequent dynamic response. The analysis of the frequency-response-function (FRF) allows the quantification of the frequency of the stimulated natural modes and, consequently, the identification of the dynamic Young modulus of the material without the need of complex support systems, elaborate setups, or alignments (ASTM E1876-21).
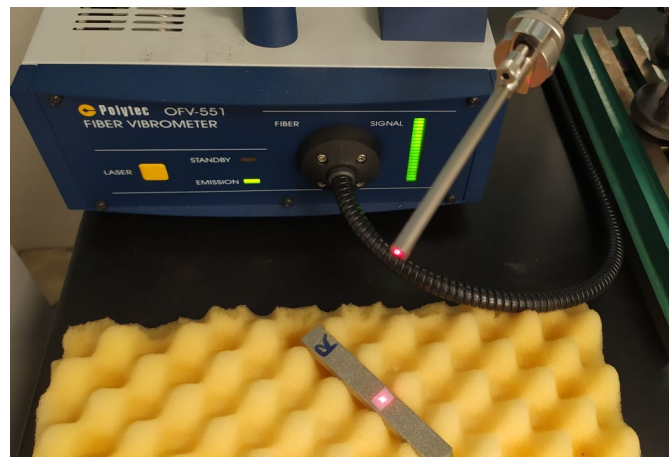

Figure 2: Ping test experimental setup.

In the present study, an impulsive excitation was applied through a lab hammer, and the dynamic response of the specimen was measured using a laser optic-fiber vibrometer (Polytec OFV 551, maximum sampling rate 50 kHz). The specimen was instrumented using a reflective stamp and was supported using a foam bed, allowing it to vibrate freely according to any combination of its natural modes (Fig. 2). The test was repeated 5 times for each specimen considered. The dynamic response was processed using a Fast Fourier Transform (FFT) to identify the natural frequency of the first bending mode f_r, which can be directly correlated to the Young modulus.

The Young modulus was identified using an accurate 3-D Finite Element Model (FEM) reproducing the first bending mode of the specimen. The material was modeled as linear elastic, homogeneous, and isotropic, taking the measured density ($\rho = 7968$ kg/m^3) and the nominal Poisson's ratio ($\nu = 0.3$) as fixed inputs. The proposed approach neglects the effect of the material porosity, usually limited when evaluating a bulk property such as the Young modulus, and of the well-known anisotropic behavior due to the building direction of the L-PBF process, which should not affect the evaluation of E. Once the FEM was set up, the Young modulus was obtained through a parametric analysis to match the natural frequency calculated experimentally for each specimen.

Fatigue tests.
The HCF tests consisted of axial fatigue tests performed at room temperature on a RUMUL Mikrotron resonant testing machine. The load ratio considered was equal to 0.05 for all the tests performed, regardless of the productivity parameters adopted. The tests were conducted on round specimens in the surface as-built conditions, designed according to the ASTM E466 standard. The main result of HCF tests was given by the fatigue resistance at 10^6 cycles $\Delta\sigma$.

Results and discussion

Tensile tests results.
The comparison between the tensile tests of the specimens obtained with different process parameters in as-built conditions is reported in Fig. 3. As E_d is reduced (i.e., the productivity is increased), the material exhibits a less ductile behavior (Fig. 3 (b)). In addition, all the tensile curves are characterized by the absence of a well-defined elastic part (evident for small strains), plausibly due to the high residual stresses present in the specimens (of the order of GPa), making the estimation of the Young modulus particularly complex (difference between the secant and tangent modulus in the elastic region), as well as dispersed. Additionally, it is difficult to distinguish between the dispersion of the Young modulus due to the measurement method and due to the production process using the tensile tests.
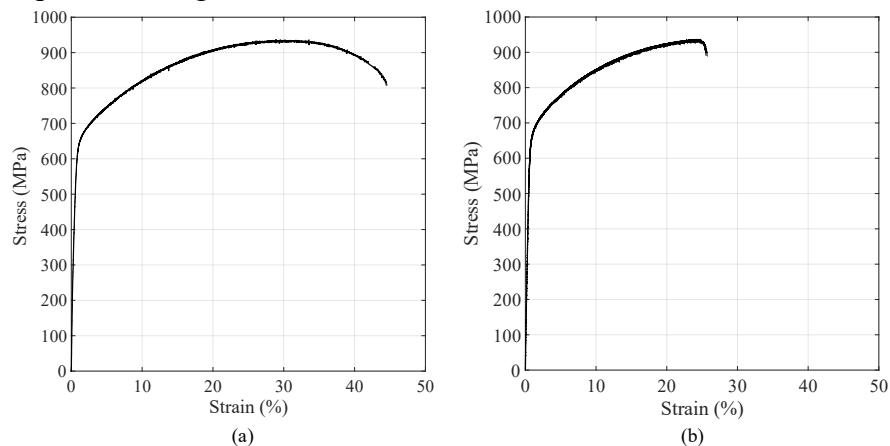

Figure 3: Tensile test results with different process parameters [11]. (a) Baseline. (b) A$_5$.

Table 3. Young modulus obtained using tensile tests [11].

	Baseline	A_2	A_3	A_5
E [GPa]	139 ± 7	142 ± 8	138 ± 7	135 ± 5

Table 3 shows the average Young modulus, together with the associated standard deviation, obtained using tensile tests as a function of the process parameters. It can be noticed that the Young modulus slightly decreases as the E_d is reduced, despite the difference between the baseline and the A_5 parameters being 2.8% of the average value.

Ping tests results.

The Young modulus estimated using the ping tests is represented as a function of the energy density in Fig. 4 and shown in Tab. 4.

In the as-built conditions, the Young modulus shows a high dependency on the energy density and increases as the energy density decreases. Moreover, the Young modulus reaches a plateau for $E_d < 46$ J/mm^3, corresponding to a 33% increase compared to the baseline value. The specimens obtained at lower energy density show a reduced Young modulus dispersion due to the manufacturing process, while the Young modulus obtained with the baseline parameters is affected by a high variability linked to the manufacturing process, with a maximum variation equal to approximately 7% of the mean value.

The peculiar static behavior obtained can be explained by considering the microstructure variations related to the production process: adopting lower energy density values realizes a more severe thermal cycle (i.e., higher thermal transfer and faster cooling) which produces a finer, and consequently stiffer, microstructure [6]. Two examples of metallographies are reported in Fig. 10, showing that a full dense material can be obtained even at higher productivity and (qualitatively) the different influence of columnar structures.
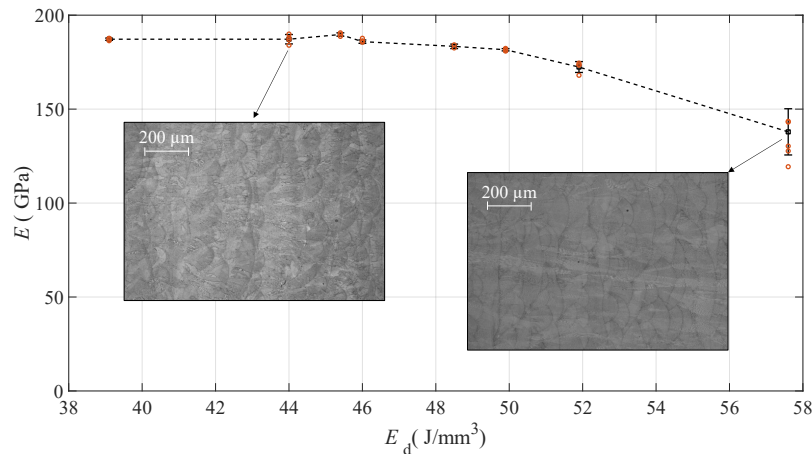

Figure 4: Young modulus obtained using ping tests and metallographies for two process parameters sets.

Table 4. Young modulus obtained using ping tests.

	Baseline	A_0	A_1	A_2	A_3	A_4	A_5	A_6
E [GPa]	137.9 ± 12.3	172.4 ± 2.9	181.6 ± 0.6	183.4 ± 1.2	189.7 ± 0.9	185.9 ± 0.9	187.2 ± 2.5	187.2 ± 0.6

Static results comparison.

The static results obtained show a different trend produced by the Young modulus estimation methods. In the case of tensile tests, the estimate is intrinsically affected by a strong dispersion due to the measurement uncertainties and the linear part stress limit introduced in the fitting

procedure, producing a lower and almost constant estimate of E characterized by high measurement dispersion. On the contrary, the ping tests produce a more reliable estimation of the Young modulus by exploiting the tangent at the origin to the tensile curve (small oscillations), and the measurement dispersion is null. The tensile tests allow to measure several material properties, but are inadequate to study the Young modulus variations and dispersion due to the technological parameters adopted (i.e., the elastic modulus of the specimens is measured instead).

Fatigue results comparison.

In Fig. 5, the fatigue strength at 10^6 cycles (Table 5) is compared with Young's modulus obtained using the ping tests and the arithmetical mean deviation of the profile heights as a function of the energy density. Apart from the baseline parameters, E and $\Delta\sigma$ show a reduced dispersion at each combination of the productivity parameters adopted. Notwithstanding the increased surface roughness at higher productivity parameters, $\Delta\sigma$ is almost constant with E_d (maximum variation with respect to the mean value 6%) and has an opposite trend compared to E. $\Delta\sigma$ reaches a minimum point (instead of a maximum) at $E_d = 45.4$ J/mm^3. On the other hand, Young's modulus obtained in as-built conditions is highly dependent on the energy density (maximum variation 30%).

The results obtained through static and HCF tests suggest the possibility of using the material in as-built conditions, achieving excellent mechanical performances depending on the productivity parameters adopted. The fatigue strength of the material shows a limited dependence on the energy density, while Young's modulus has higher values at lower energy densities. In other words, in the case of stiffness-designed components, it is possible to use higher productivity parameters to obtain a more rigid material with almost no influence on its fatigue strength.
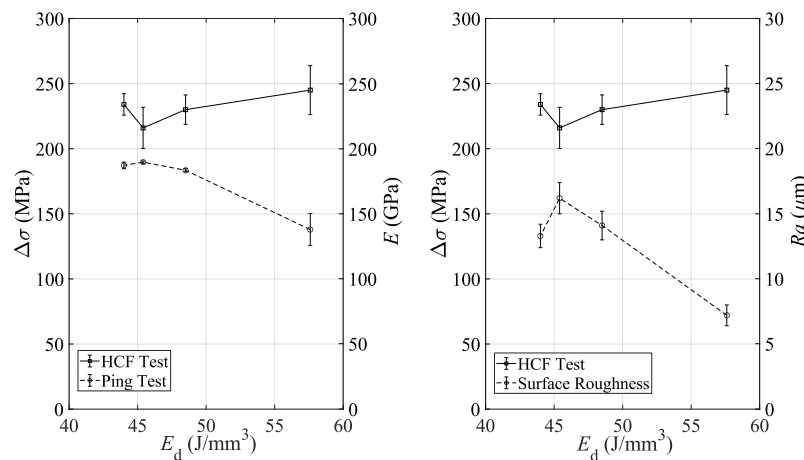

Figure 5: *Fatigue results comparison as a function of E_d. (a) $\Delta\sigma$ and E. (b) $\Delta\sigma$ and Ra.*

Table 5. *Fatigue strength at 10^6 cycles for several productivity parameters [11].*

$\Delta\sigma$ [MPa]	Baseline	A_2	A_3	A_5
As-built	245 ± 18.8	230 ± 11.3	216 ± 15.8	234 ± 8.2

Conclusions

In the present study, the influence of the energy density on the mechanical properties of specimens obtained by Laser-Powder Bed Fusion (L-PBF) is characterized. The process parameters adopted were estimated using first-order analytical models to avoid defects such as lack of fusion, keyhole, or melt pool instability. Furthermore, two dimensionless parameters were derived to describe the feasible region of the process and choose the parameter combinations to be studied.

The surface roughness parameters were measured using a profilometer, and three mechanical tests were used to identify the Young modulus and fatigue strength of the printed specimens as a

function of the energy density. The results obtained show that, as the energy density decreases, the material presents different features compared to those obtained using the baseline process parameters. In particular, adopting lower values of energy density (corresponding to more severe thermal cycles) leads to a worse surface finish and a finer material microstructure. From a mechanical point of view, this leads to a significant Young modulus increase, quantified using the ping tests in the as-built conditions, accompanied by a negligible fatigue strength reduction. Several combinations of process parameters can be adopted to increase the process productivity while achieving different mechanical properties.

In conclusion, the mechanical properties of the material obtained through L-PBF depend on several physical phenomena. The Young modulus mainly depends on the material microstructure, while the fatigue strength shows a limited dependence on the surface roughness and the contour parameters adopted. Therefore, it becomes fundamental to choose the most suitable combination of process parameters not only to avoid classic defects or increase the process productivity but also to emphasize the effects of certain consolidation processes. Without constraints on the surface roughness or fatigue strength, the energy density adopted can be reduced, obtaining stiffer components at higher process productivity. The higher and lower energy densities produce the same fatigue strength, and the eventual worsening of the surface finish can be compensated with the refinement of the material's microstructure. Finally, the surface roughness can be minimized by adopting the highest energy density values.

References

[1] Liu S., Qin C., Zong R., Fang X.: The effect of energy density on texture and mechanical anisotropy in selective laser melted Inconel 718. Materials and Design 191 (2020). https://doi.org/10.1016/j.matdes.2020.108642

[2] Balbaa M., Mekhiel S., Elbestawi M., McIsaac J.: On selective laser melting of Inconel 718: Densification, surface roughness, and residual stresses. Materials and Design 193 (2020). https://doi.org/10.1016/j.matdes.2020.108818

[3] Tucho W., Cuvillier P., Sjolyst-Kverneland A., Hansen V.: Microstructure and hardness studies of Inconel 718 manufactured by selective laser melting before and after solution heat treatment. Materials Science and Engineering A 689 (2017). https://doi.org/10.1016/j.msea.2017.02.062

[4] Calandri M., Yin S., Aldwell B., Calignano F., Lupoi R., Ugues D.: Texture and microstructural features at different length scales in Inconel 718 produced by selective laser melting. Material 12 (2019). https://doi.org/10.3390/ma12081293

[5] Facchini M., Magalini L., Robotti E., Molinari A., Höges S., Wissenbach K.: Ductility of a Ti-6Al-4V alloy produced by selective laser melting of prealloyed powders. Rapid Prototyping Journal 16 (2010). https://doi.org/10.1108/13552541011083371

[6] Guo S., Li Y., Gu J., Liu J., Peng Y., Wang P., Zhou Q., Wang K.: Microstructure and mechanical properties of Ti6Al4V/ B4C titanium matrix composite fabricated by selective laser melting (SLM). Journal of Materials Research and Technology 23 (2023). https://doi.org/10.1016/j.jmrt.2023.01.126

[7] Liverani E., Toschi S., Ceschini L., Fortunato A.: Effect of selective laser melting (SLM) process parameters on microstructure and mechanical properties of 316L austenitic stainless steel. Journal of Materials Processing Technology 249 (2017). https://doi.org/10.1016/j.jmatprotec.2017.05.042

[8] Wu H., Ren J., Huang Q., Zai X., Liu L., Chen C., Liu S., Yang X., Li R.: Effect of laser parameters on microstructure, metallurgical defects and property of AlSi10Mg printed by selective laser melting. Journal of Micromechanics and Molecular Physics 2 (2017). https://doi.org/10.1142/S2424913017500175

[9] Scime L., Beuth J.: Melt pool geometry and morphology variability for the Inconel 718 specimens produced by additive manufacturing including notch effects. Fatigue and Fracture of Engineering Materials and Structures 43 (2020). https://doi.org/10.1016/j.addma.2019.100830

[10] Moda M., Chiocca A., Macoretta G., Monelli BD., Bertini L.: Technological implications of the Rosenthal solution for a moving point heat source in steady state on a semi-infinite solid. Materials & Design 223 (2022). https://doi.org/10.1016/j.matdes.2022.110991

[11] Macoretta, G., Bertini, L., Monelli, B.D., Berto, F.: Productivity-oriented SLM process parameters effect on the fatigue strength of Inconel 718. International Journal of Fatigue 168 (2022). https://doi.org/10.1016/j.ijfatigue.2022.107384

[12] Rosenthal D.: The Theory of Moving Sources of Heat and Its Application to Metal Treatments. Transactions ASME 43 (1946). https://doi.org/10.1115/1.4018624

[13] Ravichander BB., Amerinatanzi A., Moghaddam NS.: Study on the effect of powder-bed fusion process parameters on the quality of as-built In718 parts using response surface methodology. Metals 10 (2020). https://doi.org/10.3390/met10091180

[14] Ma XFF., Zhai HLL., Zuo L., Zhang WJJ., Rui SSS., Han QNN.: Fatigue short crack propagation behavior of selective laser melted Inconel 718 alloy by in-situ SEM study: Influence of orientation and temperature. International Journal of Fatigue 139 (2020). https://doi.org/10.1016/j.ijfatigue.2020.105739